Flexible, free-standing and holey graphene paper for high power supercapacitors

Guillermo A. Ferrero, Marta Sevilla, and Antonio B. Fuertes*

Instituto Nacional del Carbón (CSIC), P.O. Box 73, Oviedo 33080, Spain

*Corresponding author: abefu@incar.csic.es

Abstract

Flexible supercapacitors based on bendable electrodes have aroused much interest for integration in clothing materials and portable electronic devices. However, simultaneous achievement of high areal energy and high power densities still presents a great challenge. Herein we report the fabrication of free-standing, flexible graphene papers suitable for high-performance flexible supercapacitors. The binder-free graphene paper is made up of two types of holey graphene units (*i.e.* wrinkled graphene sheets and graphene nanoscrolls) that produce closely interconnected, porous 3D graphene architectures. The graphene papers reported here can be fabricated with a variety of thicknesses and areal densities, in the 10-70 μm and 1-5 mg cm^{-2} ranges respectively. They exhibit a remarkable electrochemical performance in aqueous electrolytes: a) a high cell areal capacitance (230-190 mF cm^{-2} in H_2SO_4 and 180-170 mF cm^{-2} in Li_2SO_4, b) an outstanding capacitance retention of 60 % at ultra-large current densities of 1200 mA cm^{-2}, c) an excellent long-term cycling stability and d) high areal power (~280 mW cm^{-2}) and energy densities (~32 and ~60 μWh cm^{-2} in H_2SO_4 and Li_2SO_4 respectively). These highly flexible graphene papers show a great improvement, in terms of areal energy-power densities, in relation to the state-of-the-art graphene-based film electrodes.

Keywords: graphene paper, flexible, free-standing, supercapacitor, gel electrolyte.

Introduction

The storage of energy in flexible and robust supercapacitors (SCs) has generated widespread interest in relation to their integration in clothing materials and in portable electronic equipment.[1] These flexible systems must combine a high electrochemical performance with good mechanical properties such as compactness, lightness and a high resistance when being folded and bent. SCs with these properties require flexible electrodes. In contrast, electrodes in conventional supercapacitors, made up of porous carbon particles agglomerated with the aid of a binder, are rigid and, in consequence, are unsuitable for use in flexible systems. Therefore, a great deal of effort has been directed towards finding suitable materials for the fabrication of carbon-based flexible electrodes. Carbon nanotubes and carbon fibres have been investigated for this purpose.[2] However, graphene-based materials have been attracting more and more attention due to the fact that the 2D structure of graphene sheets is especially appropriate for producing flexible films without the need for any binder. Accordingly, in recent years numerous reports focussed on the fabrication of graphene-based flexible electrodes for supercapacitors have appeared in the literature.[3] Basically, two synthesis strategies have been adopted, one consisting in the incorporation of graphene sheets into flexible substrates such as cellulose-based fabrics or papers.[4] The other involves the fabrication of free-standing graphene films following different procedures such as: a) the vacuum filtration of a graphene suspension,[5] b) casting graphene onto a polished surface [6] or iii) the mechanical compression of graphene hydrogels or aerogels.[7] The use of free-standing graphene films as SC

electrodes is the most advantageous as it avoids the need for foreign inactive materials, such as supporting substrates or binders, which add complexity to the fabrication process of the SC device and have the effect of reducing the electrochemical performance if the mass or volume of the SC is taken into account.

The vacuum filtration of graphene suspensions is a straightforward and versatile procedure for obtaining free-standing graphene films. The graphene sheets are assembled in parallel to the filter membrane because two-dimensional structures are mechanically too unstable to support themselves on edges.[8] Unfortunately, the natural stacking of graphene layers is enhanced by π-π interactions, which dramatically reduces the available surface area and severely limits the diffusion of ionic species owing to the reduction of pore interconnectivity. Li *et al*. discovered that solvent molecules can be used as an effective “spacer” that keeps the graphene sheets separated and notably improves the electrochemical performance of the solvated graphene films with respect to dry films.[5a] This discovery has led to the fabrication of different types of solvated graphene films for use as electrodes in SCs.[5a, 5b, 6a, 7b-d, 8] However, the employ of free-standing graphene films in a solvated state requires a careful handling and storage. As a way to overcome these difficulties, several authors have proposed different procedures for fabricating graphene films in a dry state (commonly referred to as graphene papers, GPs).[5c, 6b, 7a, 9] However, although some of these GPs show high areal capacities (a high energy density) at low current densities, they fail when used as electrodes at fast charging/discharging rates,[6b, 7b, 10] probably because, under such tough conditions, the transport of ions inside the porous network of the graphene paper is highly restricted. On

the other hand, flexible/thin SCs able to achieve high areal power densities normally show a poor areal energy density (low areal capacity).[5a, 6a, 11] Therefore, the fabrication of GP-based SCs that combine a high energy with a high power density still remains to be achieved. In this work, we present a simple strategy for synthesizing free-standing, ultra-thin and highly dense graphene papers that are capable of a high performance as SCs electrodes. This strategy is based on the combined assembly of two types of graphene nanostructures (*i.e.* wrinkled sheets and nanoscrolls) which contain numerous basal nanoholes caused by the etching action of hydrogen peroxide.[7c] These GPs combine a high areal energy density with a large areal power density. The synthesis procedure yields GPs with a variety of structural properties, such as a thickness ranging between 7 μm to 65 μm, an areal density of between 0.5 mg cm^{-2} and 5 mg cm^{-2}, and a volumetric density of around 0.8-1.0 g cm^{-3}. More importantly, the supercapacitors fabricated with the GP electrodes exhibit high areal capacitances (114 mF cm^{-2}) at current densities as high as 1200 mA cm^{-2}, an excellent rate performance (60 % retention at 1200 mA cm^{-2}) and a long cycling life (retention of 96 % after 5000 cycles). What is more, these SCs are able to deliver a large amount of energy (~15 μWh cm^{-2}) at an ultra-high power density of ~ 500 mW cm^{-2}.

Results and discussion

Materials Characterization

The synthesis procedure from the aqueous dispersion of graphene onto graphene paper is schematically illustrated in Scheme 1. The fabrication process of the graphene paper consists of the following steps. First, a graphene

oxide (GO) suspension is reduced to graphene by means of hydrazine in the presence of ammonia.[12] Next, the graphene suspension is rapidly frozen by quenching it in liquid nitrogen and then it is lyophilized. The as-obtained graphene aerogel is ultralight in weight, has a density of <1 mg cm^{-3} (Figure 1a) and exhibits a very open structure made up of two types of graphene units: graphene nanoscrolls (GNS) and wrinkled graphene sheets, which are shown in Figure 1b. Both types of graphene units are closely interconnected as illustrated by the SEM images in Figure 1c and Figure S1. Subsequently, the graphene aerogel is oxidized with hydrogen peroxide and, finally, the resulting oxidized graphene suspension is filtered through a regenerated cellulose membrane. The deposited graphene film is dried and peeled off from the membrane and a free-standing graphene paper is thus obtained (see Figure 1d). This GP is flexible (Figure 1d/inset), compact (density ~ 0.8-0.9 g cm^{-3}) and it has a layered structure (Figure 1e). Furthermore, by adjusting the weight of the graphene aerogel, the thickness and the areal density of the GPs can be easily tailored in the 7-65 μm and 0.6-5 mg cm^{-2} ranges respectively (see Figure 1f).

A key point in our synthesis strategy is the use of fast freezing rates which are achieved by immersing the graphene dispersion in a liquid nitrogen bath. As a consequence, most of the graphene sheets dispersed in the ice remain isolated, which contrasts with the agglomeration of the graphene layers when the graphene dispersion is slowly frozen.[13] During the lyophilization process, the sublimation of ice takes place and, due to van der Waals interactions, a large number of isolated graphene sheets begin to scroll, which gives rise to the formation of GNS (Figure 1b and Figure S1). The topological transformation from 2D graphene sheets to 1D GNS notably reduces the degree of stacking of

the graphene and makes it possible for most of the graphene layers to conserve their individuality after lyophilization.[13] Importantly, the GNS possess a high structural stability and they retain their scroll morphology even after oxidation. In fact, the images in Figures 2a, 2b and S2 reveal that the GPs are made up of wrinkled graphene sheets (Figure 2b) interconnected by means of GNS (Figure 2b, inset). This architecture gives rise to robust, compact and free-standing films and the graphene stacking typical of conventional graphene papers is largely avoided. By contrast, when the graphene aerogel is prepared by means of slow freezing (*i.e.* by cooling in a refrigerator down to -20 ºC), the graphene units consist almost exclusively of wrinkled sheets (see Figure S3). For this reason, graphene papers prepared by oxidation with H_2O_2 of aerogels fabricated by using slow cooling rates (by freezing in a refrigerator at -20ºC) are made up almost exclusively of wrinkled graphene sheets (see Figure S4). The graphene paper is then so firmly stuck to the filtration membrane that it cannot be peeled off and, hence, it is unsuitable for producing free-standing papers.

The treatment of graphene units with H_2O_2 gives rise to the formation of numerous nanoholes in the basal plane of graphene. These in-plane nanopores are generated as a consequence of the oxidative etching of the carbon by hydrogen peroxide and they are of great importance because they considerably enhance ion-transport rates, as shown by previous works.[7c, 9c] Thus, whereas an un-oxidized sample is made up of non-porous graphene units (Figures S5a, S5b, S5c and S5d), an oxidized sample consists of holey graphene units with numerous randomly distributed nanoholes whose size increases with the concentration of H_2O_2: 1.5-2 nm (GP-2), 2.5-5 nm (GP-3) and > 7 nm (GP-5) (see Figures 2c and Figures S5f, S5g, S5h and S5i). As a consequence of the

generation of in-plane nanoholes, the specific surface area, as determined by the adsorption of methylene blue dye, increases from 260 m^2 g^{-1} for an un-oxidized sample GP-0 to 786 m^2 g^{-1} for GP-4 (Figure 2d). This result suggests that the oxidative process enhances the area accessible to ionic species, not only because of the generation of new pores, but probably also due to the opening of closed cavities. Both the unique architecture of graphene papers consisting in GNS linked by graphene sheets and the holey structure of the basic graphene units are the two main features responsible for the outstanding properties of the graphene papers presented in our work.

The chemical properties and microstructure of the graphene papers was investigated by elemental analysis, X-ray diffraction (XRD), Raman spectroscopy and X-ray photoelectron spectroscopy (XPS). The XRD patterns in Figure 3a reveal that, unlike the graphite oxide, which exhibits a sharp (*002*) diffraction peak at 9.7º (*d*-spacing: 0.91 nm), the graphene papers, independently of the degree of oxidation, show a weak broad band at around 24.7º (*d*-spacing ~ 0.36 nm). Although this band is typical of amorphous carbons, here it denotes a stacking of a small number of graphene layers (three or four as illustrated by the HRTEM images in Figures S5c and S5d). The Raman spectra in Figure 3b reveal that the (I_D/I_G) ratio, employed to evaluate the disorder in the graphene materials, is larger in the case of the graphene papers than in the GO. This can be ascribed to the generation of defects due to the formation of basal pores, which results in smaller sp^2 domains.[14] As can be seen in Table S1, the C/O ratio increases from 1.5 (GO) to 6.8 (GP-0) which indicates that a large number of oxygen groups have been removed by chemical reduction. The subsequent oxidation of the graphene paper promotes

the incorporation of new oxygen groups, as evidenced by the drop in the C/O ratio from 6.8 (GP-0) to 3.2 (GP-4). The incorporation of these O-groups is important because they can improve the wettability of the electrodes in the supercapacitor. The nature and distribution of the O-groups incorporated into the graphene sheets was further investigated by XPS (Figure 3c). The deconvoluted C1s spectra corresponding to the graphene papers (*i.e.* GP-0 and GP-3) reveal the presence of a certain number of O-groups at 287.1 eV (C-O, ~ 8 %), 288.6 eV (C=O, ~ 8 %) and 290.3 eV (O-C=O, ~ 3 %), besides sp^2 C (284.4 eV, 55 %), sp^3 C (285.7 eV, 24 %) and π-π^* shake-up satellite (291.98 eV, ~ 2 %).[15] In contrast, the GO contain numerous oxygen-containing functional groups at 286.6 eV (C-O, 52 %) and 288.1 eV (O-C=O, 12 %). While the numbers of oxygen groups increases, the electrical conductivity of graphene papers decreases from 23 S m^{-1} (GP-0) to 3.5 S m^{-1} (GP-4) because of the disruption of the π-system (sp^2 bounds).

Electrochemical Performance

The as-obtained graphene papers were utilized as binder-free electrode materials in symmetric supercapacitors. Aqueous electrolytes, namely 1 M H_2SO_4 and 1 M Li_2SO_4, were used to build the supercapacitors. Ion diffusion dynamics within the graphene papers subjected to different degrees of oxidation was evaluated by means of EIS analysis in the discharged state using open circuit voltage. Figure 4a shows the corresponding Nyquist plots and Figure 4b the frequency-dependence of capacitance in H_2SO_4 electrolyte. A long 45° Warburg region indicative of hindered ion motion is clearly distinguishable in the un-oxidized non-porous graphene paper, *i.e.* GP-0, which gives rise to an equivalent distributed resistance (EDR) of 11 Ohm. However, after the oxidation

treatment, the length of the Warburg region decreases to the extent that it almost disappears in the graphene papers subjected to higher degrees of oxidation, indicating an enhancement of the transport of ions through the in-plane nanoholes present in the oxidized graphene sheets. Improved wettability due to the introduction of oxygen functionalities during the oxidation treatment may also contribute to ion diffusion in the GPs. Because of this, the value of EDR decreases to 1.7 Ohm for GP-1 and 0.11 Ohm for GP-3. This translates into an ultra-fast frequency response of 220 ms for GP-3, in contrast to 11.1 s for GP-0. The slower frequency response of the sample with the highest degree of oxidation, *i.e.* GP-4, may be attributed to lower electronic conductivity, which increases the equivalent series resistance (ESR), as can be seen in the inset in Figure 4a.

The high rate capability of the holey graphene papers is also borne out by the cyclic voltammograms in Figure 4c for GP-3. It can be seen that scan rates as high as 5 V s^{-1} can be used without altering the square-shaped voltammogram typical of an EDLC. Distorted voltammograms, indicative of slower ion diffusion, are only observed for the un-oxidized graphene paper (GP-0) and the lowest oxidized paper (GP-1) at lower scan rates, as shown in Figure S6a. Importantly, a cell areal capacitance as large as ~ 100 mF cm^{-2} (electrode areal capacitance ~ 200 mF cm^{-2}) is achieved at the ultra-high scan rate of 5 V s^{-1} (see Figure 4c). Up to ~ 2 V s^{-1}, some pseudocapacitance is contributed by the abundant oxygen functionalities introduced during the oxidation treatment. As can be appreciated in Figure S6b, such redox reactions take place in the positive electrode due to the effect of the carbonyl and quinone functional groups,[16] whereas the negative electrode shows a behavior typical of an EDLC.

Figures S6b-6c also confirms the stability of the supercapacitor at a cell voltage of 1.1 V. Moreover, the charge/discharge voltage profiles at a large current density of 100 A g^{-1} in Figure 4d show only a very small voltage drop during the discharge process, confirming the low equivalent series resistance (ESR, as low as 0.32 Ohm for GP-3) of these holey graphene paper-based supercapacitors and, therefore, their superb rate capability. Indeed, as shown in Figure S6d, the holey graphene papers GP2, GP3 and GP4 withstand ultra-large current densities of 1000 mA cm^{-2} with capacitance retentions of 56, 68 and 44 %, respectively. In contrast, the non-porous graphene paper, GP-0, already shows a dramatic drop in capacitance, with a capacitance retention of only 33 % at 56 mA cm^{-2} (see inset in Figure S6d).

The ability to increase the areal density of the electrode while preserving rate capability is essential to obtain supercapacitors with high energy and high power characteristics. Hence we investigated the rate capability of supercapacitors assembled with holey graphene paper (GP-3) with different areal densities: 2 mg cm^{-2} (thickness: 30 μm), 3 mg cm^{-2} (thickness: 35 μm) and 5 mg cm^{-2} (thickness: 65 μm). As can be appreciated in Figure 4e, areal densities of ~ 2 - 3 mg cm^{-2} allow a high rate capability (*i.e.* a high power density) to be integrated with a high areal capacitance (and hence a high energy density). Indeed, ultra-large current densities of 1200 mA cm^{-2} can be achieved with cell areal capacitances of around 70 mF cm^{-2} for an areal density of 2 mg cm^{-2} and 114 mF cm^{-2} for an areal density of 3 mg cm^{-2}. To the best of our knowledge, such high areal capacitances at ultra-high rates have never been reported before and this achievement stems from the unique structure of these holey graphene papers. It is the combination of the singular structure of

the graphene paper made up of wrinkled graphene sheets and GNS that greatly reduces stacking, and the abundance of in-plane nanopores that ensures fast ion-transport rates. When the areal density is as large as 5 mg cm^{-2}, the cell areal capacitance surpasses 200 mF cm^{-2} for current densities < 100 mA cm^{-2}. However, a graphene paper with such a high areal density is unsuitable for ultra-high rate applications, as can be seen in Figure 4e. Nevertheless, the capacitance value obtained at relatively high rates (~ 100 mA cm^{-2}) is still among the highest ever reported (see Table S2). [5a, 5b, 6, 7b, 7c, 9c, 17] It is also worth noting that the graphene papers developed in this work are able to surpass all the hydrated graphene films reported so far [5a, 5b, 6, 7b, 7c, 17a, 17b] in spite of their dry state, which is a significant advantage from the point of view of assembly. Moreover, the outstanding capacitive behavior of the holey graphene papers is accompanied by a high long-term cycling stability, with a capacitance loss of only 5 % over 5000 cycles at 5 A g^{-1} (Figure 4f).

In order to increase the working voltage of the supercapacitor, 1 M Li_2SO_4 was also explored as electrolyte. As shown in Figures S7a-7b, the ion diffusion dynamics within graphene papers subjected to different degrees of oxidation follows the same trend as in H_2SO_4 (GP-4>GP-3>GP-2>GP-1>GP-0), which confirms the positive effect of in-plane nanoholes in enhancing the rate of ion transport. On the other hand, as in the case of the H_2SO_4 electrolyte, the increase in the areal density of the electrode slows down the frequency response (see the Bode plot in Figure 5a). As evidenced by the Nyquist plots in Figure 5b, the slower frequency response with increased areal density correlates directly with the enlargement of the Warburg region caused by the increase in the thickness of the electrode. Thus, the EDR value increases from

0.92 Ohm for an areal density of 2 mg cm^{-2} to 4.8 Ohm for an areal density of 5 mg cm^{-2}. Nevertheless, a comparison of the frequency response of the holey graphene paper with the highest areal density (5 mg cm^{-2}, relaxation time constant ~ 6.7 s) with that of the un-oxidized graphene paper (~ 3 mg cm^{-2}, 91 s, see Figure S7b) further verifies the contribution of the nanoholes to enhanced ion diffusion.

The galvanostatic charge/discharge voltage profiles represented in Figure 6c show that the GPs display a stable electrochemical performance in Li_2SO_4 up to a cell voltage window of 1.6 V. Regardless of the cell voltage, the coulombic efficiencies remain higher than 98 % (see inset in Figure 5c), indicating the complete reversibility of the charge storage processes involved. This stability is further confirmed by long-term galvanostatic charge/discharge cycling at 5 A g^{-1}, which shows a low capacitance loss of 5.5 % over 5000 cycles at 1.6 V (Figure 5d). The above results prove that a 45 % enlargement of the cell voltage is possible by replacing H_2SO_4 with Li_2SO_4. On the downside, as shown by Figures 5e and S7c, the rate capability of all the GPs and the areal capacitance values are lower than in H_2SO_4. The lower rate capability is attributable to the lower ionic conductivity of the Li_2SO_4 electrolyte which gives rise to an increase in both the ESR and EDR, as can be deduced by comparing the Nyquist plots in Figures 4a and 5b. On the other hand, the drop in areal capacitance in the case of Li_2SO_4 is ascribed to the lower pseudocapacitance contribution by the oxygen groups in Li_2SO_4 compared to H_2SO_4, as evidenced by the voltammograms in Figure S7d. Most important of all is that the large cell voltage of the Li_2SO_4-based supercapacitor allows a supercapacitor with higher areal energy-power characteristics, as can be appreciated from the Ragone-like plot in Figure 5f.

More specifically, at an areal power density of ~ 0.2 mW cm^{-2}, the H_2SO_4-based supercapacitor is able to provide a maximum areal energy density of ~ 32 μWh cm^{-2} compared to ~ 60 μWh cm^{-2} in the case of the Li_2SO_4-based supercapacitor, which represents a 53 % increase in the amount of energy stored when Li_2SO_4 is used as electrolyte. Only at very high power densities (~ 280 mW cm^{-2}), do both supercapacitors provide the same amount of energy (~ 16 μWh cm^{-2}) owing to the greater resistance of the Li_2SO_4-based supercapacitor compared to its H_2SO_4-based counterpart (*vide supra*).

The successful integration of high energy and high power characteristics in the GP-based supercapacitors is confirmed by the Ragone-like plot in Figure 6. Independently of the aqueous electrolyte used, the graphene paper GP-3 stores more energy and delivers it more quickly than any graphene paper/film developed so far. [4a, 5a, 5b, 6, 7b, 9c, 18] In fact, this material is even able to outperform a supercapacitor powered by an organic electrolyte, that works at a cell voltage of 2 V (trace I).[11]

To study the electrochemical performance of the graphene paper in greater depth, a solid-state flexible supercapacitor was assembled using two identical pieces of graphene paper as electrodes (GP-2, 2.7 mg cm^{-2}, 35 μm). A gel electrolyte consisting of polyvinyl alcohol (PVA)-H_2SO_4 was employed for this study. This type of electrolyte offers several advantages, such as a high flexibility, improved safety, a wide working temperature range and easy fabricability.[19] Figure 7a shows the solid-state flexible supercapacitor made up of two pieces of GP-2 of 13 mm x 26 mm. The good performance of the solid-state SC is demonstrated by the results in Figure 7b, which reveal that the areal capacitance values are only slightly lower than those of H_2SO_4 -even at high

current rates-, indicating enhanced ion diffusion in the GP when a solid electrolyte is used. The lower cell areal capacitance of this solid-state device is attributable to the fact that the transport of ions in a gel electrolyte is slower than in a liquid electrolyte such as 1 M H_2SO_4. This is confirmed by the Nyquist plots in Figure 7c. It should also be noted that this solid-state SC exhibits a large areal capacitance of 108 mF cm^{-2} for a discharge rate of 0.26 mA cm^{-2} (Figure 7b), a value which is among the best ever reported in the literature for non-hybrid supercapacitors in H_2SO_4-PVA electrolyte. [2b, 4a, 7b, 9c] Moreover, the solid-state device can work up to 100 mA cm^{-2} with a capacitance retention of 77 % (84 mF cm^{-2}). Such a high cell areal capacitance value at high rates has never been achieved before by graphene films in H_2SO_4-PVA electrolyte, as far as we are aware. [2b, 4a, 7b, 9c, 18] As a result of the high packing density of the holey graphene paper (~ 0.8 g cm^{-3}), its volumetric capacitance is around 80 % of the gravimetric one. Thereby, the solid-state device possesses a volumetric capacitance of 17 F cm^{-3} at low discharge rates and 13 F cm^{-3} at 40 A g^{-1}. This value is lower than that of a holey graphene paper (39 F cm^{-3} at 20 A g^{-1}), [9c] but higher than that of a graphene hydrogel film (8 F cm^{-3} at 1 A g^{-1}, and 6 F cm^{-3} at 20 A g^{-1}). [7b]

From a practical point of view, a solid-state SC must retain a high level of performance when bent. To verify this, we analyzed its electrochemical performance at different bending angles by performing cyclic voltammetry experiments. As can be seen in Figure 7d, the bending state does not affect the electrochemical behavior. This excellent robustness can be attributed to the exceptional mechanical strength provided by the interlinkage of graphene sheets and GNS, providing a continuous network for the transport of ions and

electrons and a stable electrolyte/electrode interface. In order to demonstrate its potential application, a red light-emitting diode (LED) with a minimum operating turn-on potential of 1.7 V was successfully powered by two supercapacitors connected in series (Figure 7e). Leakage current and self-discharge rates are also important factors for evaluating supercapacitor performance. During self-discharge processes, a small amount of leakage current will cause supercapacitors to lose voltage when they are not being used and are in a charged state. This loss of voltage could disqualify the supercapacitor for use in some commercial applications if the self-discharge rate is too high. In our solid-state device we therefore measured the time required for the voltage to change from V_{max} to ½ V_{max}, which is the voltage range in which most supercapacitors operate.[20] As shown in Figure 7f, the voltage drops from 1.1 V (V_{max}) to ½ V_{max} after 20 hours in an open circuit. This is longer than in 1 V solid-state devices constructed with graphene hydrogel films (14 hours) [7b] and holey-graphene films (12.5 hours).[9c] On the other hand, leakage current only amounts to ~ 9 μA mg^{-1} after 2 hours of maximum voltage. Although the fabrication and assembly of the solid-state supercapacitor has not been fully optimized, its electrochemical behavior, flexibility and robustness have been proved to be excellent. Optimization of certain parameters such as the pressure applied to compress the device, the properties of the gel electrolyte or the electrical contact between the current collectors and the electrodes along with the use of advanced manufacture technologies would further enhance its electrochemical performance.

Conclusions

In summary, we have presented a novel synthesis strategy for the fabrication of a graphene paper made up of two types of holey graphene units (*i.e.* wrinkled graphene sheets and graphene nanoscrolls) that give rise to a highly porous, interconnected 3D graphene architecture. The thickness and areal density of the resultant flexible graphene paper can be modulated in the range of 10-70 μm and 1-5 mg cm^{-2} respectively. This material exhibits a very open structure that provides easy access to the electrolyte solution, guaranteeing high ion-transport rates. It makes it possible for graphene paper-based supercapacitors to show a remarkable electrochemical performance with a high areal energy density and an ultra-large areal power. Consequently, the device can achieve an excellent areal capacitance (114 mF cm^{-2}) at current densities as high as 1200 mA cm^{-2}, an excellent rate performance (60 % retention at 1200 mA cm^{-2}), a long cycle life (96 % retention after 5000 cycles) and it is able to deliver a large amount of energy (~15 μWh cm^{-2}) at an ultra-high power density of ~ 500 mW cm^{-2}. Its easy fabricability and enhanced electrochemical performance would make this graphene paper reported here a promising electrode material for flexible energy storage systems.

Experimental details

Fabrication of the graphene paper

Graphene oxide (GO) was prepared by using a modified Hummer´s method as reported elsewhere. [21] The GO solid was dispersed in water by ultrasonication (Sonics, Ultrasonic Vivracell, 500 W, 40 %) for 1.5 h to make a GO aqueous dispersion with a concentration of 0.5 mg GO mL^{-1}. To prepare an aqueous graphene colloidal suspension, 120 mL of GO dispersion (0.5 mg mL^{-1}) was

mixed with 0.24 mL hydrazine (35 wt % in water, Aldrich) and 0.42 mL ammonia (30 wt %, Aldrich) in a Teflon vessel, stirred for 15 min and then treated at 100 ºC for 3 h.[12] The Teflon vessel was then immediately immersed in a nitrogen liquid in order to obtain a high freezing rate. The frozen dispersion was then transferred to a lyophilizer (Telstar Cryodos) and freeze-dried at a temperature of – 51 ºC and at a pressure of 0.06 mbar. The graphene aerogel (density < 1 mg cm^{-3}) thus obtained was dispersed in an aqueous solution of H_2O_2 (concentration: 0 - 5 wt %) and treated, under stirring, at 100 ºC (reflux) for 4 h. [7c] The graphene paper was made by the vacuum filtration of the oxidized graphene dispersion through a regenerated cellulose membrane (0.45 µm, Sartorius) followed by drying at 50 ºC. The graphene papers were denoted as *GP-x, x* being the concentration of H_2O_2 employed in the corresponding experiment.

Material Characterization

Scanning electron microscopy (SEM) images were obtained on a Quanta FEG650 (FEI) instrument, whereas transmission electron microscopy (TEM) images were recorded on a JEOL (JEM 2100-F) apparatus operating at 200 kV. The specific surface area was determined by the methylene blue adsorption method as described by McAllister et al.[22] X-ray diffraction (XRD) patterns were obtained on a Siemens D5000 instrument operating at 40 kV and 20 mA, using Cu KR radiation. The Raman spectra were recorded on a Horiva (LabRam HR-800) spectrometer. The source of radiation was a laser operating at a wavelength of 514 nm and at a power of 25 mW. X-ray photoelectron spectroscopy (XPS) was carried out on a Specs spectrometer, using Mg KR (1253.6 eV) radiation emitted from a double anode at 150 W. The dc electrical

conductivity of the graphene papers was determined using a home-made apparatus by pressing the papers between two plungers, into a hollow Nylon cylinder (inner diameter of 8 mm), and applying a pressure of 7.1 MPa. Elemental analysis (C, H, N and O) of the samples was carried out on a LECO CHN-932 microanalyzer.

Characterization of the electrochemical supercapacitors

The electrochemical measurements were performed in two-electrode Swagelok™ type cells using 1 M H_2SO_4 and 1 M Li_2SO_4 as electrolytes. The electrochemical capacitors were assembled using two graphene papers of comparable mass and thickness, electrically isolated by a glassy fibrous separator. To evaluate the polarization characteristics of the positive and negative electrodes independently, a special two-electrode cell provided with a reference electrode Hg/Hg_2SO_4 (SME, saturated) was used. The electrochemical characterization was performed using a computer-controlled potentiostat (Biologic VMP3 multichannel generator) and consisted of cyclic voltammetry experiments, electrochemical impedance spectroscopy studies (EIS) and galvanostatic charge/discharge cycling tests (CD).

Electrochemical impedance spectroscopy (EIS) measurements were performed at open circuit voltage (*i.e.* 0 V) in discharged state within the frequency range of 1 mHz to 100 kHz and a 10 mV AC amplitude. Bode plots of the dependence of the capacitance on frequency and Nyquist plots were recorded to characterize the impedance of the tested samples. The specific gravimetric capacitance of a single electrode, C_{EIS} (F g^{-1}), was calculated according to the following formula and normalized with respect to the highest specific gravimetric capacitance, *i.e.* capacitance at 1 mHz:

$$C_{EIS} = \frac{2|Im(Z)|}{2\pi f[(Im(Z))^2 + (Re(Z))^2] \cdot m} \quad (1)$$

where *f* is the operating frequency (Hz), and *Im(Z)* and *Re(Z)* are the imaginary and real components of the total device resistance (Ohm). The relaxation time constant, τ_0, which separates the capacitive and the resistive behavior of the supercapacitor, was deduced from the frequency f_0 as follows: $\tau_0 = 1/f_0$, where f_0 is obtained from the real capacitance plot at C' = $C_{1mHz}/2$. The equivalent series resistance (ESR) was calculated from the intercept of the high frequency semicircle loop with the real impedance axis at the highest frequency.[23] The equivalent distributed resistance (EDR) was determined from the linear projection of the vertical portion at low frequencies to the real axis (after subtraction of the ESR and R_i).[23b]

Cyclic voltammetry experiments (CVs) were performed between 0 and 1.1 V in H_2SO_4, and 0 and 1.6 V in Li_2SO_4 at increasing sweep rates from 1 mV s^{-1} to 10 V s^{-1}. Plots of cell areal capacitance *vs.* voltage were calculated using the formula:

$$C_{cell} = \frac{I}{\nu S} \quad (2)$$

Where I = current, ν = scan rate and S = geometrical area of the device.

Galvanostatic charge/discharge cycling was performed in the same voltage range at increasing current densities from 0.1 to 1200 mA cm^{-2}, based on the active mass of one electrode. The cell areal capacitance determined from the galvanostatic cycles was calculated by means of the formula:

$$C_{cell} = \frac{I}{(dV/dt)\ S} \quad (3)$$

where dV/dt = the slope of the discharge curve. Taking into account the dependence of specific capacitance on the voltage in the present materials due to the presence of pseudocapacitance, the selection of an appropriate voltage range for the determination of the slope is very important to avoid overestimating the specific capacitance. As most supercapacitors are operated in the range of V_{max} to approximately ½ V_{max}, the upper half of the discharge curve was used to determine the slope of the discharge curve.[20]

To trace the Ragone-like plots, the areal energy (μWh cm^{-2}) and the areal power (mW cm^{-2}) densities were calculated using the following formulae:

$$E = \frac{1}{2} C_{cell} \Delta V_d^2 \quad (4)$$

$$P = \frac{E}{\Delta t_d} \quad (5)$$

where ΔV_d is the operation voltage ($V_{max} - IR_{drop}$) and Δ_{td} is the discharge time.

Fabrication of flexible solid-state supercapacitors

The PVA/H_2SO_4 gel electrolyte was prepared as follows: 2 g of PVA (MW: ~ 9000, Aldrich) was dispersed in 20 mL H_2SO_4 1 M and, then the resulting mixture was heated up to 50 ºC under continuous stirring until the solution appeared clear (around 30 min). After that, the graphene paper electrodes (size: 13 mm × 26 mm) were immersed in H_2SO_4 1 M and dried at room temperature. In order to assemble the solid-state device, the H_2SO_4-PVA was poured onto the glassy fibrous separator. Then, the two electrodes were attached to the separator on one side and to a graphite film used as collector on the other.

Finally, the symmetric supercapacitor was fabricated by sandwiching all the components between two flexible PET films and pressing it so that the polymer gel on the separator could infiltrate into the GP.

Acknowledgments

This research work was supported by the FICYT Regional Project (GRUPIN14-102), Spanish MINECO (CTQ2015-63552-R) and Fondo Europeo de Desarrollo Regional (FEDER). G. A. F. thanks the MINECO for his predoctoral contract.

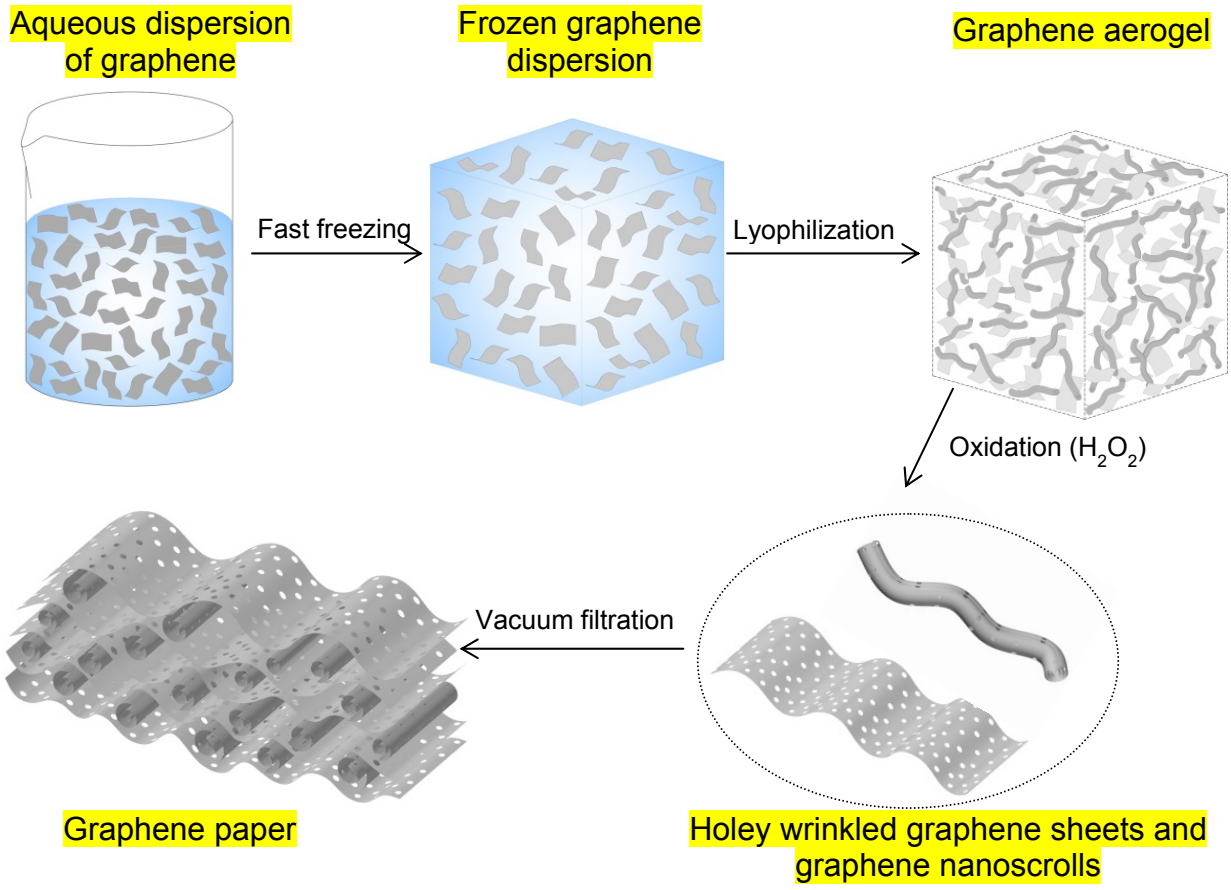

Scheme 1. Illustration of the synthesis procedure.

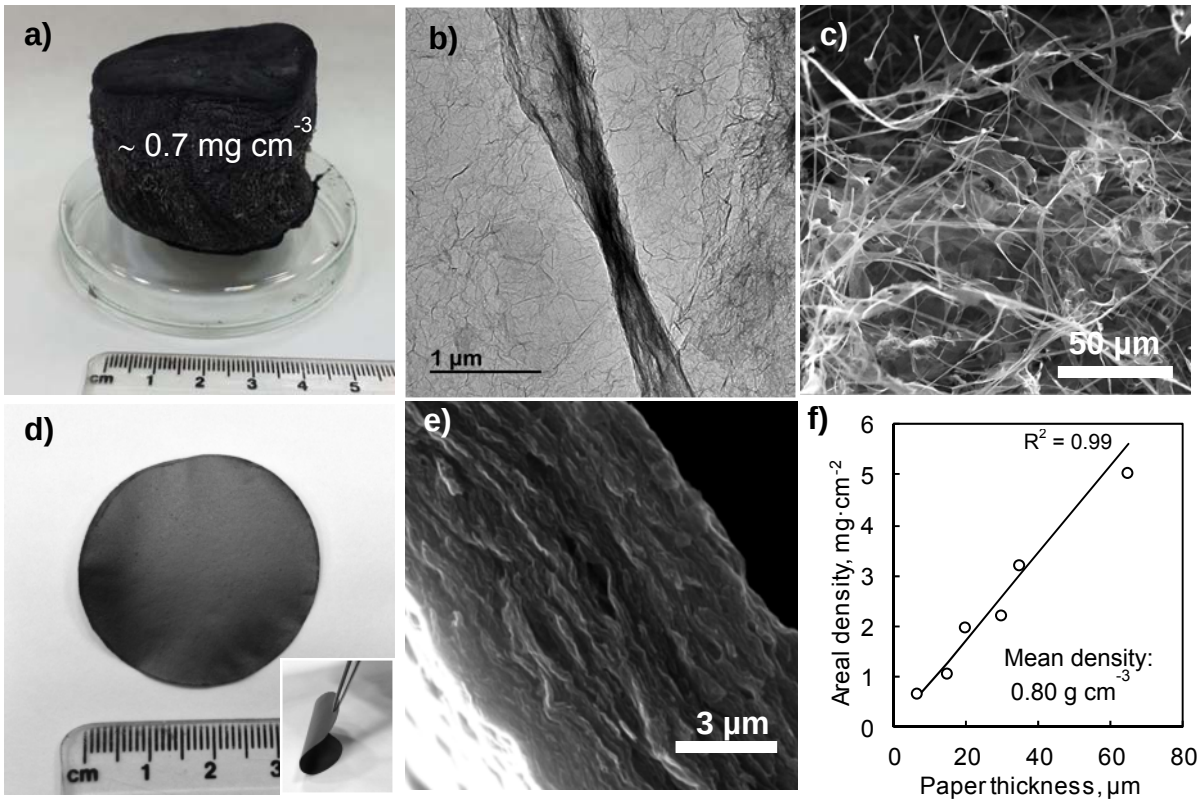

Figure 1. (a) Image of the graphene aerogel, (b) TEM images of a graphene nanoscroll superimposed on a wrinkled graphene sheet, (c) SEM microphotograph of the graphene aerogel, (d) image of the graphene paper peeled off from the filter membrane, (e) cross-section of a graphene paper, (f) modification of the thickness and the areal density of graphene paper (Ø: 37 mm) with the amount of graphene aerogel used in the synthesis.

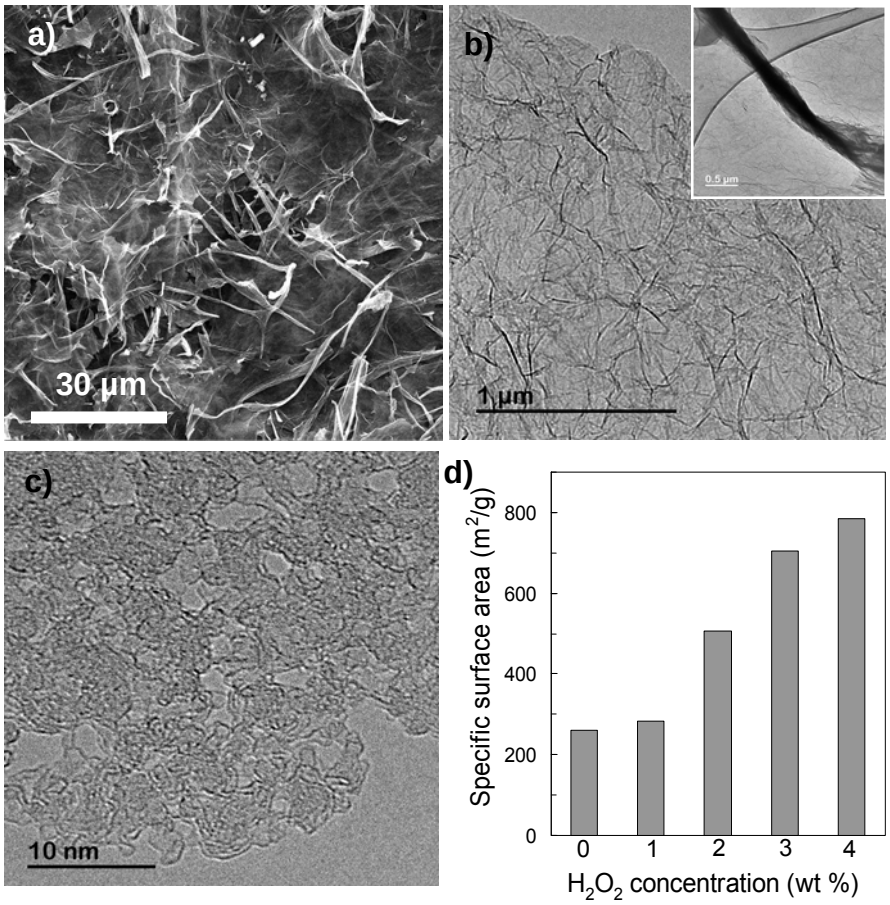

Figure 2. (a) SEM microphotograph of a graphene paper, (b) TEM images of a wrinkled graphene sheet and a graphene nanoscroll (inset) after the oxidation step, (c) HRTEM image of a graphene sheet showing the in-plane nanopores generated by oxidative etching and (d) changes in the specific surface area of the graphene paper with the degree of oxidation.

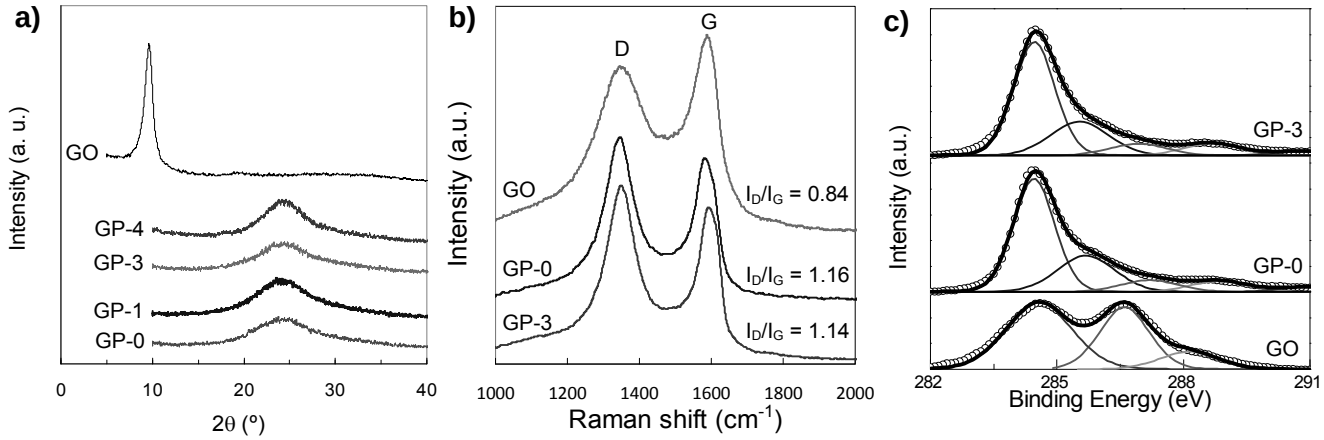

Figure 3. (a) XRD patterns, (b) Raman spectra, and (c) high-resolution XPS C1s spectra of GO and of the graphene papers GP-0 and GP-3.

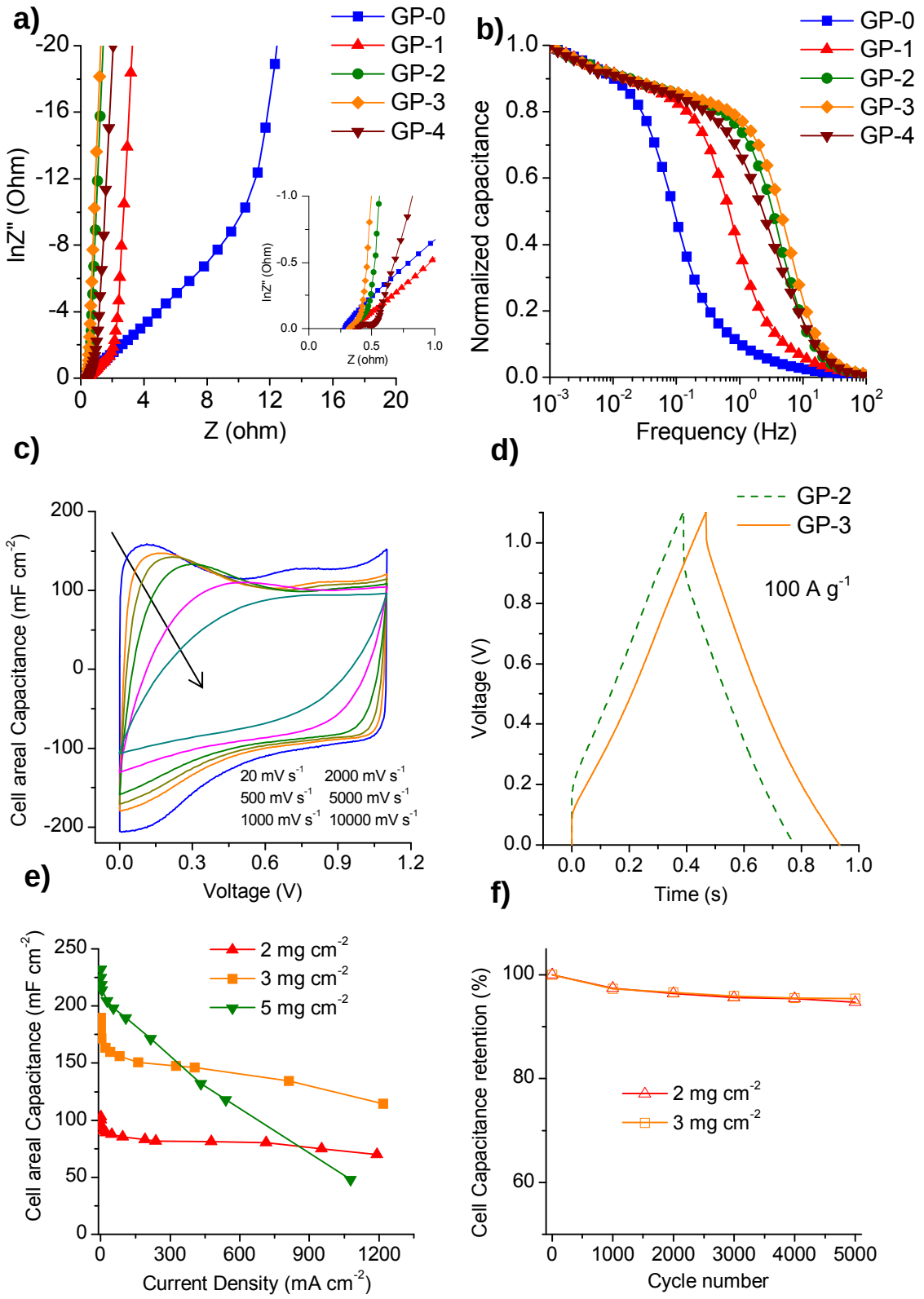

Figure 4. Electrochemical performance of the graphene paper in 1 M H_2SO_4. (a) Nyquist plot, (b) Bode plot, (c) cyclic voltammograms, d) galvanostatic charge-discharge at 100 A g^{-1}, (e) variation in areal capacitance with the current density

for GP-3 at different areal densities and (f) long-term stability of GP-3 (1.1 V, 5 A g^{-1}). In Figures 4a, 4b, 4c and 4d the areal densities are: a) GP-0, 3 mg cm^{-2}, b) GP-1, 2.7 mg cm^{-2}, c) GP-2, 2.4 mg cm^{-2}, d) GP-3, 2 mg cm^{-2} and e) GP-4, 2 mg cm^{-2}.

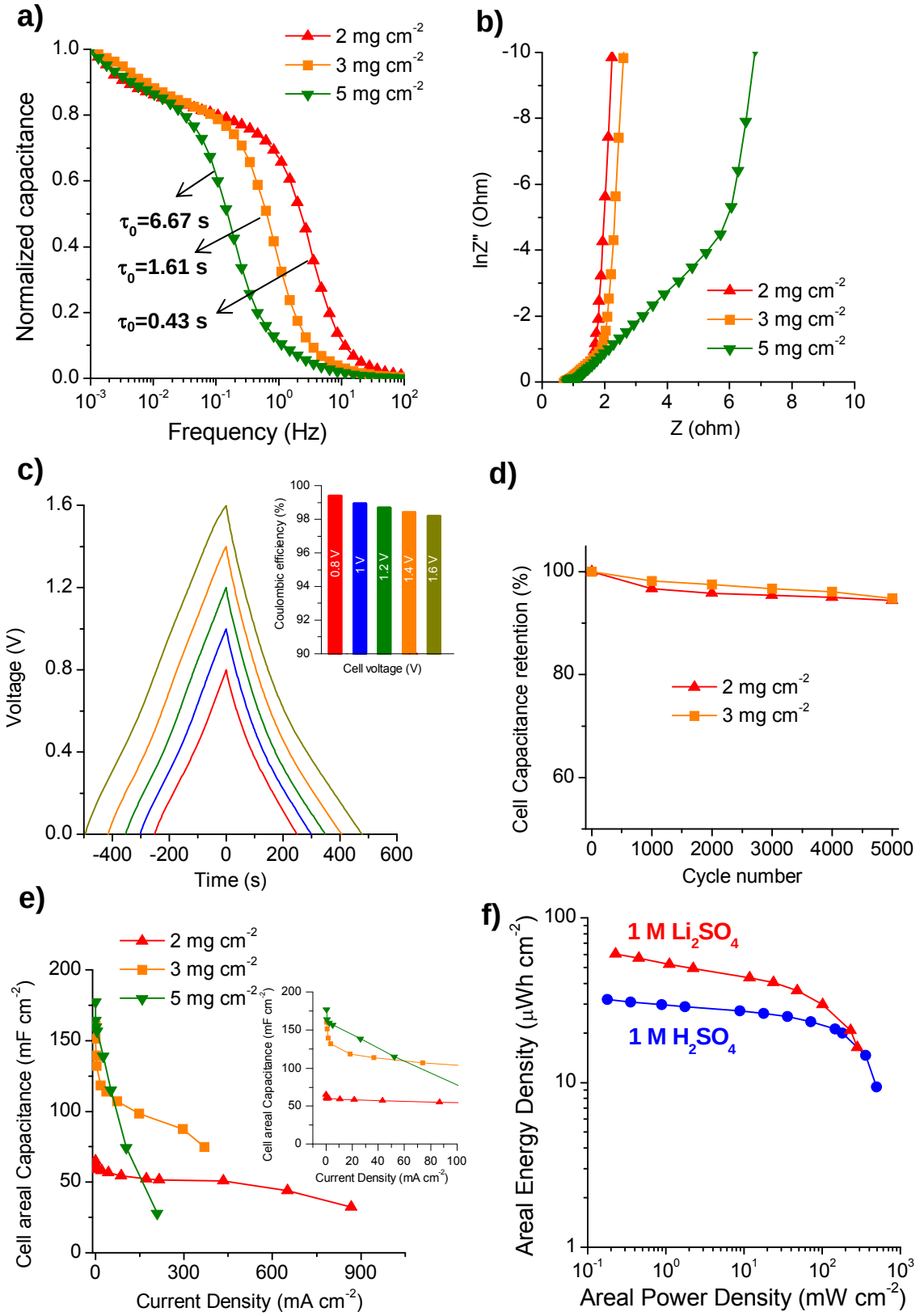

Figure 5. Electrochemical performance of the graphene paper (GP-3) in a neutral electrolyte (1 M Li_2SO_4). (a) Bode plot, (b) Nyquist plot, (c) galvanostatic

charge/discharge voltage profiles at increasing cell voltage (0.44 mA cm^{-2}) (inset: coulombic efficiency at different cell voltages), (d) long-term stability (1.6 V, 5 A g^{-1}), (e) variation in areal capacitance with increasing current density and f) Ragone plot for H_2SO_4 and Li_2SO_4 (3 mg cm^{-2}).

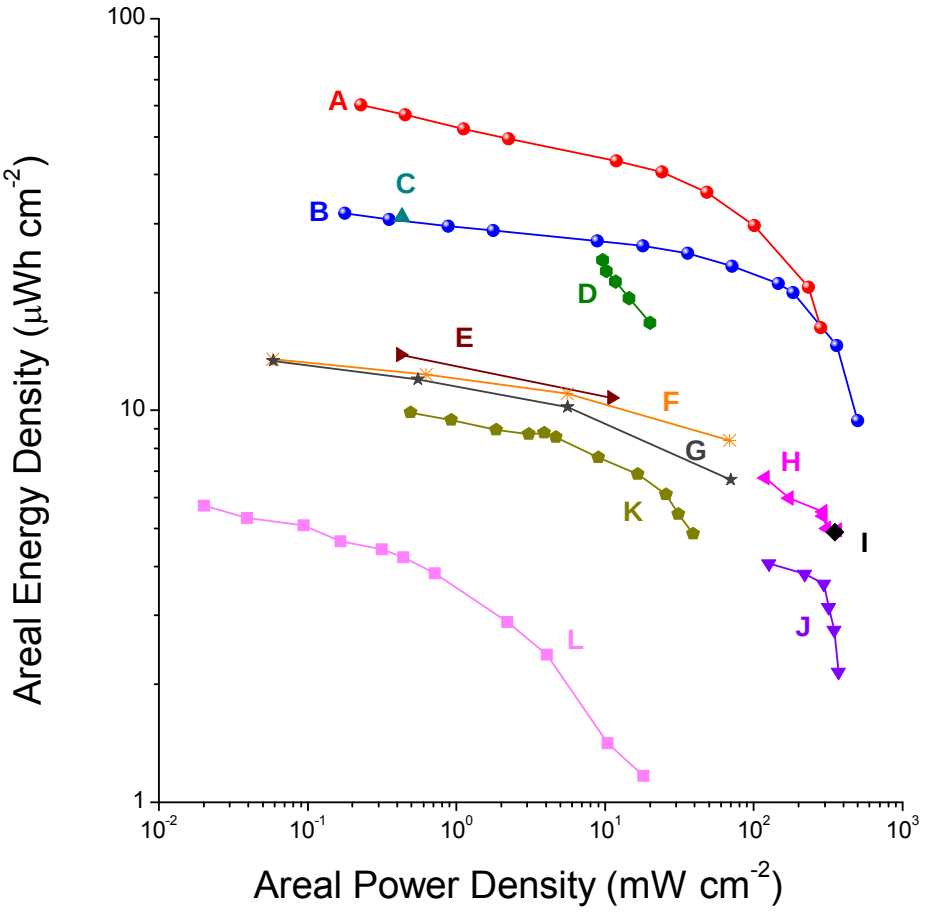

Figure 6. Ragone plot comparing the areal energy and power densities obtained for the graphene paper GP-3 (3 mg cm^{-2}, 35 μm) (A: 1 M Li_2SO_4 and B: 1 M H_2SO_4) with those obtained for other graphene-based films: C (Functionalized graphene film, 1 mg cm^{-2}), [18] D (Graphene hydrogel film, 120 μm, 2 mg cm^{-2}), [7b] E (Holey graphene paper, 9 μm, 1 mg cm^{-2}), [9c] F (Chemically converted graphene hydrogel film, 0.76 g cm^{-3}), [5b] G (Chemically converted graphene hydrogel film, 1.33 g cm^{-3}), [5b] H (Solvated graphene film, 1 mg cm^{-2}), [5a] I (Flash converted graphene, 0.35 mg cm^{-2}),[11] J (Solvated graphene film, 152 μm, 0.44 mg cm^{-2}), [6a] K (Solvated graphene film, 1 mg cm^{-2}), [6b] L (Graphene on cellulose, 0.44 mg cm^{-2}).[4a]

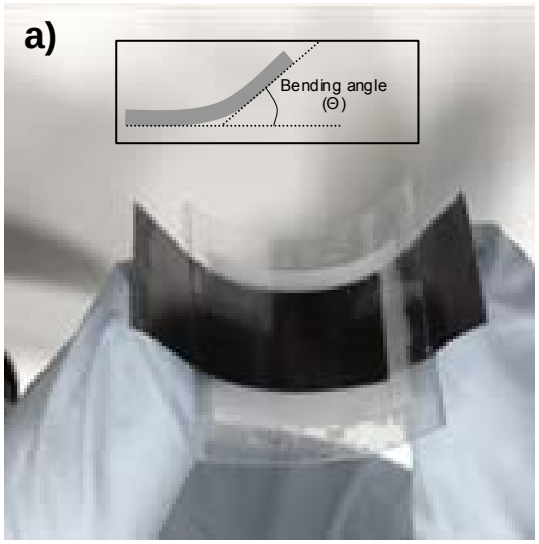
a)
Bending angle
(Θ)

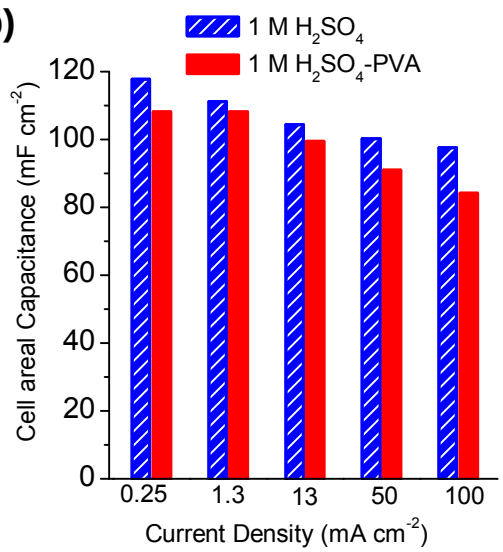
b)
1 M H2SO4
1 M H2SO4-PVA
Cell areal Capacitance (mF cm-2)
120
100
80
60
40
20
0
0.25
1.3
13
50
100
Current Density (mA cm-2)

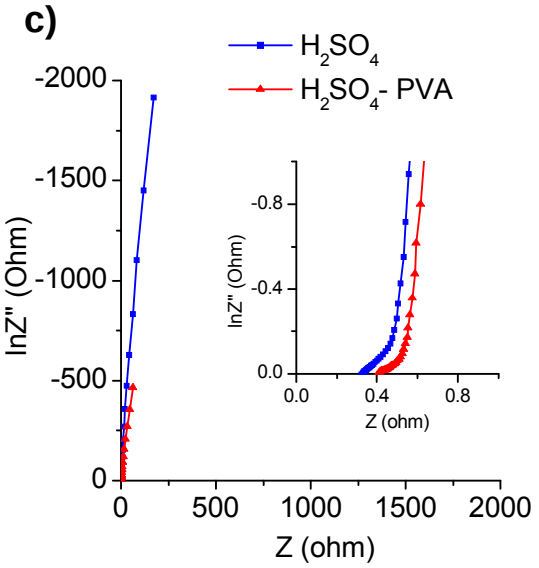
c)
H2SO4
H2SO4- PVA
-2000
-1500
-1000
-500
0
InZ'' (Ohm)
0
500
1000
1500
2000
Z (ohm)
-0.8
-0.4
0.0
InZ'' (Ohm)
0.0
0.4
0.8
Z (ohm)

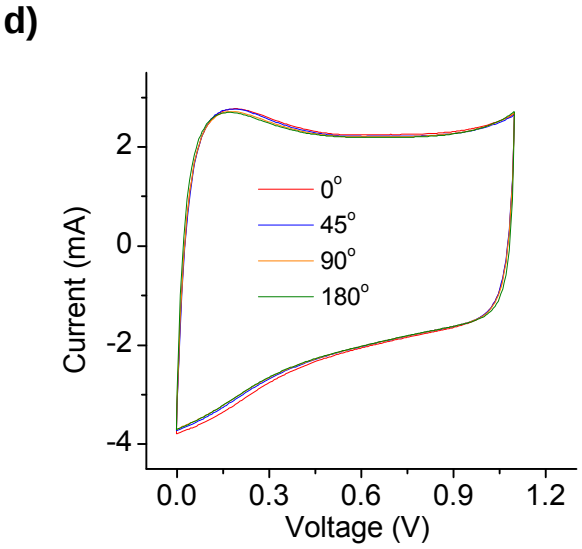
d)
2
0
-2
-4
Current (mA)
0°
45°
90°
180°
0.0
0.3
0.6
0.9
1.2
Voltage (V)

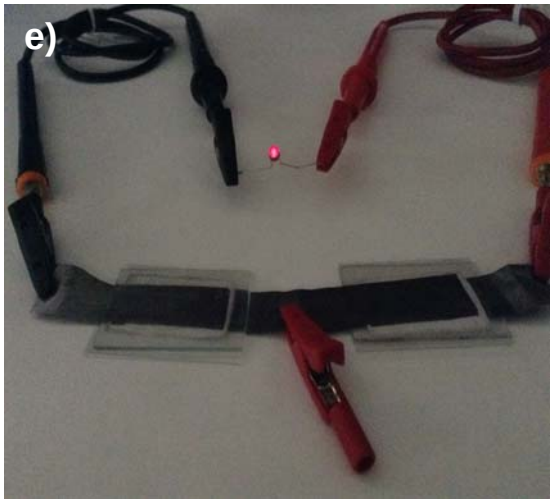
e)

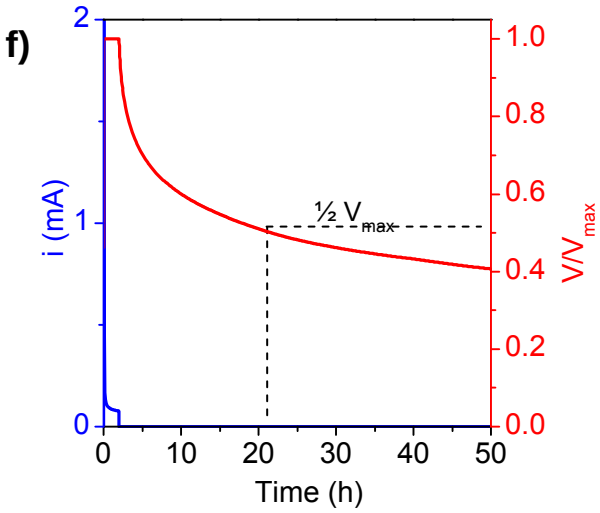
f)
2
1
0
i (mA)
½ Vmax
1.0
0.8
0.6
0.4
0.2
0.0
V/Vmax
0
10
20
30
40
50
Time (h)

Figure 7. Electrochemical performance of the GP-based solid-state flexible supercapacitor. (a) Image of the flexible solid-state supercapacitor device (inset shows a schematic definition of a bending angle); (b) rate dependence of the areal capacitance, (c) Nyquist plots corresponding to the H_2SO_4 and H_2SO_4-PVA electrolytes, (d) cyclic voltammograms at 5 mV s^{-1} of the flexible solid-state supercapacitor at different bending angles from 0° to 180°; (e) a red LED lightened by two flexible supercapacitors connected in series and (f) leakage current and self-discharge of the solid-state flexible supercapacitor at 1.1 V of cell voltage. Electrode material GP-2.

References

1. a) X. Lu, M. Yu, G. Wang, Y. Tong and Y. Li, *Energy Environ. Sci.* **2014**, *7*, 2160-2181; b) Y.-Z. Zhang, Y. Wang, T. Cheng, W.-Y. Lai, H. Pang and W. Huang, *Chem. Soc. Rev.* **2015**, *44*, 5181-5199; c) X. Peng, L. Peng, C. Wu and Y. Xie, *Chem. Soc. Rev.* **2014**, *43*, 3303-3323; d) D. Ghosh and S. O. Kim, *Electronic Materials Letters* **2015**, *11*, 719-734.
2. a) Y. J. Kang, S.-J. Chun, S.-S. Lee, B.-Y. Kim, J. H. Kim, H. Chung, S.-Y. Lee and W. Kim, *ACS Nano* **2012**, *6*, 6400-6406; b) G. Wang, H. Wang, X. Lu, Y. Ling, M. Yu, T. Zhai, Y. Tong and Y. Li, *Adv. Mater.* **2014**, *26*, 2676-2682; c) L.-F. Chen, Z.-H. Huang, H.-W. Liang, W.-T. Yao, Z.-Y. Yu and S.-H. Yu, *Energy Environ. Sci.* **2013**, *6*, 3331-3338; d) K. Song, W.-L. Song and L.-Z. Fan, *J. Mater. Chem. A* **2015**, *3*, 16104-16111; e) K. Yu Jin, C. Haegeun, H. Chi-Hwan and K. Woong, *Nanotechnology* **2012**, *23*, 065401.
3. Y. Shao, M. F. El-Kady, L. J. Wang, Q. Zhang, Y. Li, H. Wang, M. F. Mousavi and R. B. Kaner, *Chem. Soc. Rev.* **2015**, *44*, 3639-3665.
4. a) Z. Weng, Y. Su, D.-W. Wang, F. Li, J. Du and H.-M. Cheng, *Adv. Energy Mater.* **2011**, *1*, 917-922; b) L. Liu, Z. Niu, L. Zhang, W. Zhou, X. Chen and S. Xie, *Adv. Mater.* **2014**, *26*, 4855-4862; c) W.-w. Liu, X.-b. Yan, J.-w. Lang, C. Peng and Q.-j. Xue, *J. Mater. Chem.* **2012**, *22*, 17245-17253.
5. a) X. Yang, J. Zhu, L. Qiu and D. Li, *Adv. Mater.* **2011**, *23*, 2833-2838; b) X. Yang, C. Cheng, Y. Wang, L. Qiu and D. Li, *Science* **2013**, *341*, 534-537; c) Z. Niu, J. Chen, H. H. Hng, J. Ma and X. Chen, *Adv. Mater.* **2012**, *24*, 4144-4150.
6. a) U. N. Maiti, J. Lim, K. E. Lee, W. J. Lee and S. O. Kim, *Adv. Mater.* **2014**, *26*, 615-619; b) Z. Xiong, C. Liao, W. Han and X. Wang, *Adv. Mater.* **2015**, *27*, 4469-4475.
7. a) F. Liu, S. Song, D. Xue and H. Zhang, *Adv. Mater.* **2012**, *24*, 1089-1094; b) Y. Xu, Z. Lin, X. Huang, Y. Liu, Y. Huang and X. Duan, *ACS Nano* **2013**, *7*, 4042-4049; c) Y. Xu, Z. Lin, X. Zhong, X. Huang, N. O. Weiss, Y. Huang and X. Duan, *Nat Commun* **2014**, *5*; d) M. Sevilla, G. A. Ferrero, T. T. Vu and A. B. Fuertes, *ChemNanoMat* **2016**, *2*, 33-36.
8. C. Cheng and D. Li, *Adv. Mater.* **2013**, *25*, 13-30.
9. a) G. Wang, X. Sun, F. Lu, H. Sun, M. Yu, W. Jiang, C. Liu and J. Lian, *Small* **2012**, *8*, 452-459; b) B. G. Choi, J. Hong, W. H. Hong, P. T. Hammond and H. Park, *ACS Nano* **2011**, *5*, 7205-7213; c) Y. Xu, C.-Y. Chen, Z. Zhao, Z. Lin, C. Lee, X. Xu, C. Wang, Y. Huang, M. I. Shakir and X. Duan, *Nano Letters* **2015**, *15*, 4605-4610.
10. A. Sumboja, C. Y. Foo, X. Wang and P. S. Lee, *Adv. Mater.* **2013**, *25*, 2809-2815.
11. L. J. Wang, M. F. El-Kady, S. Dubin, J. Y. Hwang, Y. Shao, K. Marsh, B. McVerry, M. D. Kowal, M. F. Mousavi and R. B. Kaner, *Adv. Energy Mater.* **2015**, *5*, n/a-n/a.
12. D. Li, M. B. Muller, S. Gilje, R. B. Kaner and G. G. Wallace, *Nat Nano* **2008**, *3*, 101-105.
13. Z. Xu, B. Zheng, J. Chen and C. Gao, *Chemistry of Materials* **2014**, *26*, 6811-6818.
14. a) S. Stankovich, D. A. Dikin, R. D. Piner, K. A. Kohlhaas, A. Kleinhammes, Y. Jia, Y. Wu, S. T. Nguyen and R. S. Ruoff, *Carbon* **2007**, *45*, 1558-1565; b) Z.

Lin, G. Waller, Y. Liu, M. Liu and C.-P. Wong, *Adv. Energy Mater.* **2012**, *2*, 884-888.

15. a) H. Darmstadt, C. Roy and S. Kaliaguine, *Carbon* **1994**, *32*, 1399-1406; b) S. Biniak, G. Szymański, J. Siedlewski and A. Świtkowski, *Carbon* **1997**, *35*, 1799-1810.
16. a) V. Ruiz, C. Blanco, E. Raymundo-Piñero, V. Khomenko, F. Béguin and R. Santamaría, *Electrochim. Acta* **2007**, *52*, 4969-4973; b) M. P. Bichat, E. Raymundo-Piñero and F. Béguin, *Carbon* **2010**, *48*, 4351-4361.
17. a) X. Feng, W. Chen and L. Yan, *Nanoscale* **2015**, *7*, 3712-3718; b) J. Zang, C. Cao, Y. Feng, J. Liu and X. Zhao, *Sci. Rep.* **2014**, *4*, 6492; c) W. Lv, Z. Li, G. Zhou, J.-J. Shao, D. Kong, X. Zheng, B. Li, F. Li, F. Kang and Q.-H. Yang, *Adv. Funct. Mater.* **2014**, *24*, 3456-3463; d) Y. Bai, X. Yang, Y. He, J. Zhang, L. Kang, H. Xu, F. Shi, Z. Lei and Z.-H. Liu, *Electrochim. Acta* **2016**, *187*, 543-551.
18. Y. Xu, Z. Lin, X. Huang, Y. Wang, Y. Huang and X. Duan, *Adv. Mater.* **2013**, *25*, 5779-5784.
19. M. Li, Z. Tang, M. Leng and J. Xue, *Adv. Funct. Mater.* **2014**, *24*, 7495-7502.
20. M. D. Stoller and R. S. Ruoff, *Energy Environ. Sci.* **2010**, *3*, 1294-1301.
21. W. Lv, D.-M. Tang, Y.-B. He, C.-H. You, Z.-Q. Shi, X.-C. Chen, C.-M. Chen, P.-X. Hou, C. Liu and Q.-H. Yang, *ACS Nano* **2009**, *3*, 3730-3736.
22. M. J. McAllister, J.-L. Li, D. H. Adamson, H. C. Schniepp, A. A. Abdala, J. Liu, M. Herrera-Alonso, D. L. Milius, R. Car and R. K. Prud'homme, *Chemistry of Materials* **2007**, *19*, 4396-4404.
23. a) C. Portet, P. L. Taberna, P. Simon, E. Flahaut and C. Laberty-Robert, *Electrochim. Acta* **2005**, *50*, 4174-4181; b) R. Kötz and M. Carlen, *Electrochim. Acta* **2000**, *45*, 2483-2498.

Graphical Abstract

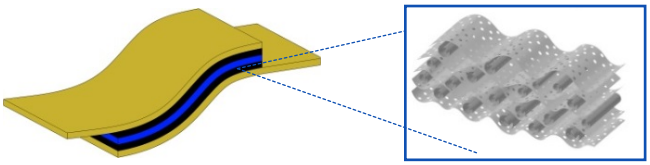

The fabrication of free-standing, flexible graphene papers for high-performance flexible supercapacitors is herein presented. The binder-free graphene paper, made up of wrinkled graphene sheets and graphene nanoscrolls, can be fabricated with a variety of thicknesses and areal densities. The graphene-based supercapacitor integrates both high areal energy and high power densities in aqueous electrolytes.